Hindawi
International Journal of Photoenergy
Volume 2024, Article ID 2676368, 11 pages
https://doi.org/10.1155/2024/2676368

Research Article

ZnO/NiO Nanocomposite with Enhanced Photocatalytic H_2 Production

Muhammad Hashim,[1] **Muhammad Usman**,[1] **Sohail Ahmad**,[1] **Rasool Shah**,[2] **Atizaz Ali**,[1] **and Naveed Ur Rahman**[3]

[1]*Department of Physics, Abdul Wali Khan University Mardan, Mardan, KPK, Pakistan*
[2]*Department of Computer Science and Mathematics, Lebanese American University, Beirut, Lebanon*
[3]*Department of Physics, Bacha Khan University, Charsadda, KPK, Pakistan*

Correspondence should be addressed to Rasool Shah; rasool.shah@lau.edu.lb

Received 6 November 2023; Revised 3 January 2024; Accepted 2 February 2024; Published 15 February 2024

Academic Editor: Adel A. Ismail

Copyright © 2024 Muhammad Hashim et al. This is an open access article distributed under the Creative Commons Attribution License, which permits unrestricted use, distribution, and reproduction in any medium, provided the original work is properly cited.

Inorganic photocatalytic materials exhibiting a highly efficient response to ultraviolet-visible light spectrum have become a subject of widespread global interest. They offer a substantial prospect for generating green energy and mitigating water pollution. Zinc oxide (ZnO), among various semiconductors, proves advantageous for water-splitting applications due to its elevated reactivity, chemical stability, and nontoxic nature. However, its efficacy as a photocatalyst is hindered by limited light absorption capacity and swift charge carrier recombination. To improve charge separation and enhance responsiveness to ultraviolet-visible light photocatalysis, the formation of a heterojunction with another suitable semiconductor is beneficial. Thus, we employed hydrothermal route for the synthesis of the samples, which is a high-pressure method. The formations of ZnO/NiO heterostructures were revealed by scanning electron microscopy, X-ray diffraction analysis, energy-dispersive X-ray spectroscopy, and Fourier transform infrared spectroscopy. The nanocomposites were discovered to have a substantially higher photocatalytic activity for the generation of H_2. The H_2 production rates show that ZnO (i.e., 168.91 $\mu mol g^{-1} h^{-1}$) exhibits good H_2 production rates as compared to NiO (i.e., 135.74 $\mu mol g^{-1} h^{-1}$). The best production rates were observed for ZN-30 (i.e., 247.56 $\mu mol g^{-1} h^{-1}$) which is 1.46 times greater than ZnO and 1.82 times greater than NiO. This enhanced photocatalytic activity for ZN-30 is because of the good electron-hole pair separation due to the formation of depletion layer, suppression of fast charge recombination, and overcoming resistance corrosion.

1. Introduction

The rise in the CO_2 levels in the atmosphere has been constant for the past decades [1], reaching up to 412 ppm, causing severe damage to our ecosystem (on land as well as marine life) that is majorly caused by the extensive consumption of fossil fuels (oil, natural gas, and coil) as our primary and major source of energy [2, 3]. Therefore, it is evident that the natural carbon cycle has deteriorated and that innovative concepts for achieving sustainable and green energy sources for the future have become a need/necessity.

Therefore, H_2 as a fuel with no carbon footprint might be considered the most suitable energy source for the future [4]. Earth consists of large percentage of water that can be utilized for the production of H_2 via water-splitting process [5]. The photocatalysts are utilized in the process of water splitting for the production of H_2 through photocatalysis. The purpose of the photocatalyst here is to speed up the chemical reaction between the reactants (by shrinking down the activation energy) when illuminated with light.

Metal oxides are a decent candidate to be utilized as a photocatalyst, such as ZnO, SnO_2, TiO_2, NiO, CuO, MgO, and Fe_2O_3 [6–8]. But metal oxides reside some properties, i.e., corrosion resistance, fast charge (e^-/h^+ pair) recombination, and wide band gap [9], which are not in favor of efficient photocatalysis; therefore, we need to overcome these problems and engineer these properties to our favor. In order to overcome these hurdles, three solutions are available, i.e., doping, variation in morphology, and heterojunctions.

Titanium dioxide (TiO_2) is one of the semiconductor metal oxide photocatalysts that has undergone substantial research and is frequently employed [10–12]. Due to the similar band gap energies ranging from 3.10 to 3.37 eV (from nanostructure-bulk structure) and lower price of zinc oxide (ZnO), it is a viable substitute for titanium dioxide (TiO_2) [13–16]. The low quantum yield of ZnO is due to the high rate of photogenerated electron-hole pair recombination [17]. According to several studies, the mutual transfer of photogenerated charge carriers (e^-/h^+) in the ZnO-based heterojunctions can enhance the photocatalytic activity of the heterojunction, including noble metal and semiconductor heterojunctions [18–22].

NiO with an intriguing electronic structure is a p-type semiconductor with a rock salt or cubic structure comprising of a band gap ranging from 3.6 to 4.0 eV (nanostructure-bulk structure). Nickel oxide, among the composite materials, has drawn a steadily increased interest with its ZnO/NiO heterostructural nanomaterials [23, 24]. NiO is capable of being utilized for the fabrication of n-p heterojunction with ZnO because of its strong hole (h^+) mobility and low lattice mismatch [25, 26].

Yousaf et al. [27] synthesized NiO/ZnO nanocomposite photocatalyst through coprecipitation and cogel formation methods, utilizing the precipitating agents KOH, Na_2CO_3, and $H_2C_2O_4$. The most efficient NiO/ZnO composite sample demonstrated superior photocatalytic activity compared to that of the individual components, thus establishing its greater efficiency than the pure components. Udayachandran Thampy et al. [28] synthesized a nanocomposite of ZnO–NiO and documented its efficiency in photocatalytic degradation. The material was produced using the sonication method applied to their corresponding salts. The research revealed that the ZnO–NiO composite displayed superior degradation efficiency compared to individual metal oxides when exposed to solar light. This enhanced efficiency was linked to the internal electric field existing between the ZnO and NiO phases. Sharma et al. [29] synthesized nanostructured ZnO–NiO-mixed oxide powder exhibiting enhanced photocatalytic performance using a homogeneous precipitation method, followed by high-temperature annealing within the 300–700°C range. Convenient chemical pathways described in existing literature for crafting ZnO–NiO nanocomposites involve one-pot solution processing followed by high-temperature annealing (300–700°C) and a solvothermal process requiring an extended process duration of 12 hours. Ma et al. [30] synthesized ZnO–NiO nanocomposites by combining neem leaf extract with a hydrothermal synthesis method. Jayababu et al. [31] fabricated ZnO–NiO nanocomposites through a coprecipitation technique followed by a sol-gel process. Xiao et al. [32] documented an innovative approach to produce ZnO–NiO nanoheterojunctions using a three-step chemical synthesis method. In this process, hydrothermally synthesized carbon spheres served as the substrates for the development of these heterostructures. The final step involved the high-temperature calcination (at 400°C), leading to the thermal evaporation of the carbon spheres.

In the current study, we outline an efficient and cost-effective approach for the fabrication of ZnO (nanoplateletes)/NiO (nanospheres) heterostructures. A systematic study has been conducted on the photocatalytic activity of ZnO/NiO heterojunctions. According to the results, a type two heterojunction (staggered bap) has been achieved which promotes the fast interfacial charge transfer within the heterojunction which highly promotes the photocatalytic activity [33]. Therefore, the n-type ZnO/p-type NiO heterojunctions have outstanding photocatalytic activity that outperforms that of pure ZnO and pure NiO [23].

2. Experimental Details

2.1. Materials. For the synthesis of ZnO, zinc nitrate hexahydrate ($Zn(NO_3)_2.6H_2O$), potassium hydroxide (KOH), and deionized water are the chemicals that were utilized. For the synthesis of NiO, nickel(II) chloride hexahydrate ($Ni(II)Cl_2.6H_2O$), urea (CH_4N_2O), and deionized water were utilized. And for the synthesis of ZnO/NiO heterojunction, zinc nitrate hexahydrate ($Zn(NO_3)_2.6H_2O$), potassium hydroxide (KOH), nickel(II) chloride hexahydrate ($Ni(II)Cl_2.6H_2O$), urea (CH_4N_2O), and deionized water are the chemicals utilized. All the chemicals/precursors used were of analytical grade. Hydrothermal route was adapted for the synthesis of our required samples as it helps us achieve high temperature and pressure.

2.2. Synthesis of ZnO. For the synthesis of ZnO, zinc nitrate hexahydrate ($Zn(NO_3)_2.6H_2O$) and potassium hydroxide (KOH) were measured at their stoichiometric amounts. Firstly, zinc nitrate hexahydrate (7.512 g/0.505 M) was added to 50 ml of DI water (Sol. 1) and was stirred using a magnetic stirrer. Then, potassium hydroxide (6.985 g/1.5 M) was added in 83 ml of DI water in a separate container (Sol. 2). While Sol. 1 was under stirring, a dropwise addition of Sol. 2 into Sol. 1 was carried out for 15 minutes. The resulting solution (Sol. 3) was transferred to an autoclave (200 ml), which was shifted to the oven for heat treatment at a constant temperature of 180°C for 20 hours. The resulting precipitates (of Sol. 3) were washed with DI water and ethanol (70-30%) in the centrifuge for removing the impurities. One cycle of the centrifuge was set to be at 5500 RPM for 5 minutes, and a total of 7 cycles were performed to achieve excellent purification. The samples were transferred into a China dish and were dried in the oven at 80°C for 12 hours.

2.3. Synthesis of NiO. For the synthesis of NiO, nickel(II) chloride hexahydrate ($Ni(II)Cl_2.6H_2O$) and urea (CH_4N_2O) were measured at their stoichiometric amounts. Firstly, nickel(II) chloride hexahydrate (3.565 g/0.1 M) was added to 150 ml of DI water (Sol. 1) and was stirred using a magnetic stirrer. Then, urea (1.801 g/0.2 M) was added to Sol. 1 under continuous stirring for 10 minutes. The resulting solution was transferred into an autoclave (200 ml), which was shifted to the oven for heat treatment at a constant temperature of 120°C for 12 hours. The resulting precipitates were washed with DI water and ethanol (70-30%) in the centrifuge for removing the impurities. One cycle of the centrifuge was set to be at 5500 RPM for 5 minutes, and a total of 7 cycles were performed to achieve excellent purification. The

Table 1: Sample names and corresponding compositions.

Sample name	Z100	ZN-10	ZN-20	ZN-30	ZN-40	N100
ZnO%	100	90	80	70	60	—
NiO%	—	10	20	30	40	100

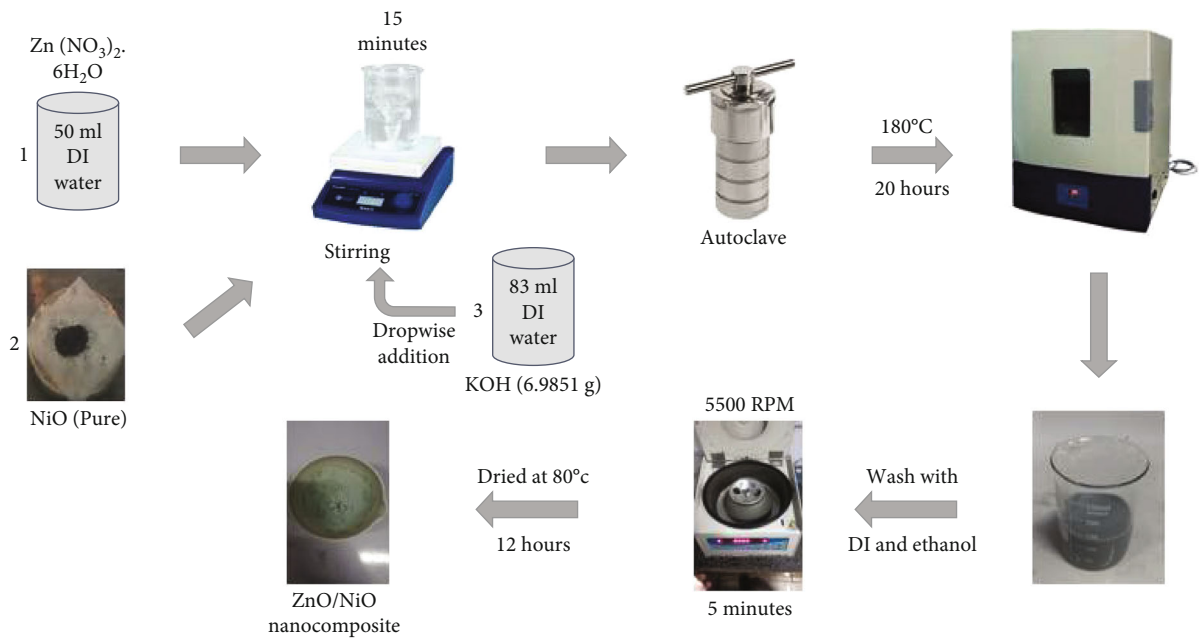

Figure 1: Hydrothermal synthesis of ZnO/NiO heterojunction.

samples were transferred into a China dish and were dried in the oven at 60°C for 12 hours. The samples were annealed in the furnace for curing at 500°C° for 2 hours at a 5°C rise per minute.

2.4. Synthesis of ZnO/NiO Heterojunction. A total number of 6 samples were synthesized as demonstrated in Table 1: ZnO (pure), NiO (pure), ZnO/NiO heterojunction (90% ZnO/ 10% NiO denoted by ZN-10), ZN-20, ZN-30, and ZN-40. The general synthesis procedure for the heterojunction is shown in Figure 1, described as stoichiometric amounts of NiO (pure), zinc nitrate hexahydrate ($Zn(NO_3)_2.6H_2O$), and potassium hydroxide (KOH) employed. Firstly, zinc nitrate hexahydrate was added in DI water (Sol. 1) and was stirred using a magnetic stirrer. Then, potassium hydroxide was added in DI water in a separate container (Sol. 2). While Sol. 1 was under stirring, NiO (pure) and a dropwise addition of Sol. 2 into Sol. 1 was carried out for 15 minutes. The resulting solution (Sol. 3) was transferred to an autoclave, which was shifted to the oven for heat treatment at a constant temperature of 180°C for 20 hours. The resulting precipitates (of Sol. 3) were washed with DI water and ethanol (70-30%) in the centrifuge for removing the impurities. One cycle of the centrifuge was set to be at 5500 RPM for 5 minutes, and a total of 7 cycles were performed to achieve excellent purification. The samples were transferred into a China dish and were dried in the oven at 80°C for 12 hours.

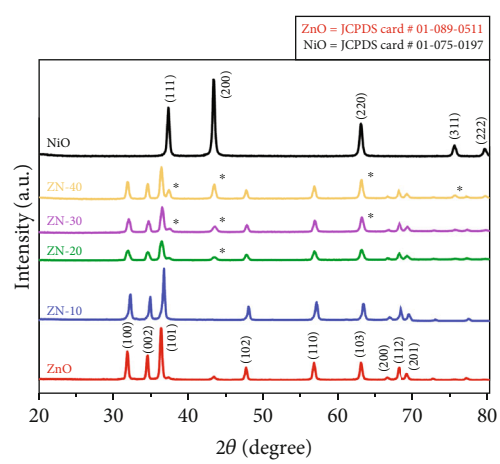

Figure 2: XRD analysis.

2.5. Characterization. The crystal structure and phase of the samples were studied using JDX-3532 (JEOL, Japan) diffractometer. The morphology and elemental composition of our samples were studied using JSM5910 by JEOL, Japan, with EDX attachment (INCA200/Oxford Instruments, UK). For studying the nature and behavior of the chemical bonds in the samples, Cary 630 (Agilent Technologies, USA) was employed. Shimadzu UV-1800 UV-visible scanning spectrophotometer was utilized to examine the material's optical

Table 2: Lattice parameters.

S. no.	Peak positions 2θ (degree)	Crystallite size (nm)	d-spacing (Å)	Microstrain ($\times 10^{-3}$)
ZnO				
1	31.93609	23.33	2.8001	5.4
2	34.60013	25.61	2.5903	4.55
3	36.42891	23.74	2.4644	4.67
4	47.731	25.05	1.9039	3.42
5	56.78595	23.45	1.6199	3.11
6	63.05414	23.07	1.4731	2.87
7	66.54924	23.71	1.3254	2.85
8	68.14391	22.7	1.3755	2.73
9	69.27856	22.72	1.3552	2.68
		Average crystallite size = 24.04 nm		
NiO				
1	37.39984	22.12	2.4026	4.89
2	43.43758	21.42	2.0816	4.37
3	63.0341	19.79	1.4735	3.35
4	75.57161	19.59	1.2572	2.89
5	79.56295	19.31	1.2039	2.81
		Average crystallite size = 20.39 nm		
ZN-30				
1	32.12396	17.61	2.7841	7.11
2	34.76413	18.44	2.5785	6.29
3	36.58046	16.9	2.4545	6.54
4	43.57221	12.77	2.0755	7.32
5	47.84529	18.88	1.8996	4.53
6	56.89828	18.47	1.617	3.94
7	63.16263	16.76	1.4709	3.95
8	68.24632	17.51	1.3731	3.53
9	69.38185	14.54	1.3534	4.19
		Average crystallite size = 17.18 nm		

properties. The photoluminescence examination was carried out using FS5 spectrofluorometer (Edinburgh Instruments).

2.6. Electrochemical Impedance Spectroscopy. The EIS analysis was adapted to study how the photogenerated charge carriers are stimulated and transported within our crystalline material. The EIS analysis was carried out with the help of an electrochemical cell, which consisted of Na_2SO_3 solution along with three electrodes, i.e., working, counter, and reference electrode. For the preparation of our working electrode, we employed FTO (fluorine tin oxide) substrate (1×1 cm). Initially, the substrate was divided into two sections; one section was covered with a masking tape, and on the other section, our sample (10 mg), Nafion solution (250 μl), and ethylene glycol (250 μl) were deposited and dried in the oven. When the substrate was dried, the masking tape on the other half of the substrate was removed and was ready for use. As the electrochemical cell was ready for use, light was illuminated on the experimental setup which caused the photogenerated charge carriers in the working electrode to move, and therefore, change in the potential due to our sample with respect to the reference electrode was measured.

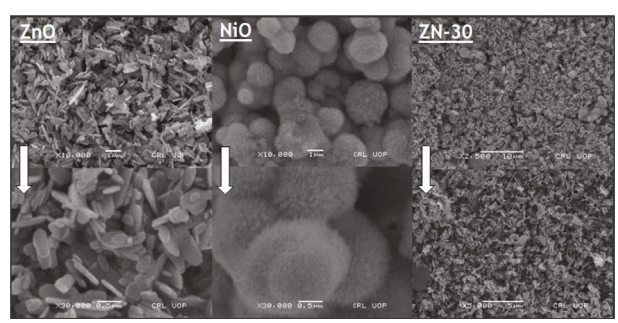

(a) (b) (c)

Figure 3: SEM micrographs of (a) ZnO, (b) NiO, and (c) ZN-30.

2.7. Gas Chromatography. In the experimental procedure of photocatalysis, a mixture of gases was obtained which needed to be separated in order to obtain our required gas (H_2). The sample was injected into the oven through the

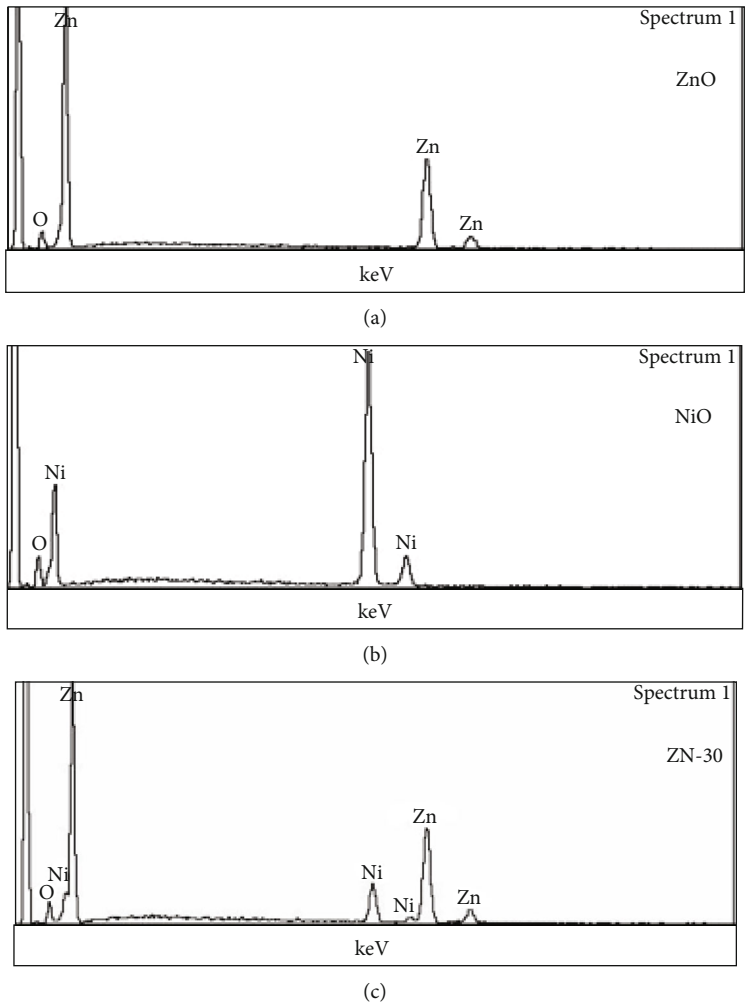

Figure 4: EDX analysis of (a) ZnO, (b) NiO, and (c) ZN-30.

injector port. As the temperature of the injector port was kept at 20-50 C° higher than that of the oven, it helped our sample to be rapidly volatilized. The volatilized sample was moved within the column of the oven with the help of a carrier gas. As different gases have different boiling points, they move with different speeds within the column. The gases having low boiling point move quickly, while the gases having higher boiling points move relatively slow, after which they reach the detector and provide us the data.

3. Results and Discussions

3.1. XRD Characterization. XRD analysis was adapted to study the crystal structure and phase of the synthesized samples. The diffraction peaks for ZnO, NiO, ZN-10, ZN-20, ZN-30, and ZN-40 are obtained in the XRD micrograph shown in Figure 2. The diffraction peaks 31.93609°, 34.60013°, 36.42891°, 47.731°, 56.78595°, 63.05414°, 66.54924°, 68.14391°, and 69.27856° for ZnO at 2θ values correspond to (100), (002), (101), (102), (110), (103), (200), (112), and (201) crystal faces, therefore revealing a hexagonal wurtzite structure while being identical to the JCPDS card # 01-089-0511 [34]. For NiO, the diffraction peaks 37.39984°, 43.43758°, 63.0341°, 75.57161°, and 79.56295° at 2θ values correspond to (111), (200), (220), (311), and (222) crystal faces, therefore revealing a cubic structure while being identical to the JCPDS card # 01-075-0197 [35]. The XRD pattern of both ZnO and NiO indicates high crystallinity which can be seen from the diffraction peaks. Similar for the nanocomposites, the peaks of both ZnO and NiO are present (indicated by a star in Figure 2) indicating the presence of both crystal structures (hexagonal wurtzite and cubic) and the successful formation of our required heterojunction. The lattice parameters shown in Table 2 reveal the average crystallite sizes for ZnO, NiO, and ZN-30 to be 24.04 nm, 20.39 nm, and 17.18 nm, respectively.

3.2. SEM Analysis. By employing scanning electron microscopy, the surface morphology of ZnO, NiO, and ZN-30 was examined. The micrographs of ZnO, NiO, and ZN-30 samples are shown in Figure 3. The first set of micrographs of ZnO and NiO was captured with 1 μm magnification and ×10,000 resolution, and for ZN-30, 10 μm magnification and ×2,500 resolution were adjusted. For the second set of micrographs, for ZnO and NiO, 0.5 μm magnification and ×30,000 resolution were adapted, and for ZN-30, 5 μm magnification and ×5,000 resolution were adjusted. The

difference between the scale of pure ZnO, NiO, and the heterojunction was adapted due to the difference between the grain size of ZnO and NiO. The grain size of NiO is very large as compared to that of ZnO, and different scales are adapted for the sake of comparability. From the SEM micrographs, we conclude that ZnO nanoplatelete morphology and NiO nanosphere morphology are observed whereas for ZN-30 heterojunction, both the morphologies, i.e., nanoplatelets on the surface of nanosphere morphology, are observed.

3.3. EDX Analysis. For the study of elemental composition of the samples, EDX analysis is adapted, according to which the presence of Zn and O for ZnO is detected. For NiO, the presence of Ni and O is clearly observed, whereas for ZN-30 heterojunction, the presence of Zn, Ni, and O is clearly confirmed as shown in Figures 4(a)–4(c). The micrographs and the quantitative analysis of EDX study clearly indicate that there are no impurities present in all the samples, therefore indicating high purity of the synthesized samples. From the quantitative analysis (Table 3), the emissions from the specific orbits of ZnO (i.e., O (L) and Zn (L)), NiO (O (K) and Ni (K)), and ZN-30 (O (K), Ni (K), and Zn (L)) along with their respective weight % and atomic % values are indicated.

3.4. FTIR Analysis. For studying the behavior of the chemical bonds present in the synthesized samples, the FTIR spectra of ZnO, NiO, and ZN-30 were captured. From the analysis, a common broad peak in the spectra of ZnO, NiO, and ZnO/NiO heterojunctions is observed from 3200 to 3600 cm^{-1}, which is due to the O-H stretching bond. For ZnO at 568 cm^{-1}, the stretching vibrations of Zn-O are observed, and the existence of a band at 1242 cm^{-1} corresponds to the H–O–H bending mode, whereas the OH stretching mode is observed at 3428 cm^{-1}. These vibrations stem from water molecules adsorbed on the surface of the crystallites [36]. For NiO, the presence of an absorption band at 3497 cm^{-1} in the sample indicates the absorption of the OH stretching mode. Additionally, the existence of a band at 1235 cm^{-1} (corresponding to the H–O–H bending mode) is indicative of water absorption in the NiO product. It is crucial to highlight that the IR spectra of NiO with a spherical shape exhibited a pronounced and robust vibration band at 575 cm^{-1}, arising from the stretching vibration of metal-oxygen bonds [37]. For ZN-30, the IR absorption bands observed at 563 cm^{-1} correspond to ZnO, while those at 570 cm^{-1} resemble the characteristics of NiO nanocomposite. Additionally, the characteristic bands of both components are merged. These findings validate the presence of ZnO and NiO and their presence in the heterojunctions and support the XRD data. Figure 5 shows the FTIR spectrum of ZnO, NiO, and their heterojunctions, while Table 4 provides the quantitative analysis of the samples.

3.5. UV-Vis Analysis. For the synthesized samples, UV-visible absorption spectrum was captured for the analysis of their optical properties. For ZnO, NiO, and ZN-30, the UV-visible absorption spectra were measured between 200 and 800 nm as shown in Figure 6(a). According to the absorption spectra (Figure 6(a)), the absorption peaks for

Table 3: EDX quantitative analysis.

Element	Weight %	Atomic %
ZnO		
O (L)	9.55	30.14
Zn (L)	90.45	69.86
NiO		
O (K)	2.49	8.57
Ni (K)	97.51	91.49
ZN-30		
O (K)	4.04	14.18
Ni (K)	29.49	32.08
Zn (L)	66.47	53.74

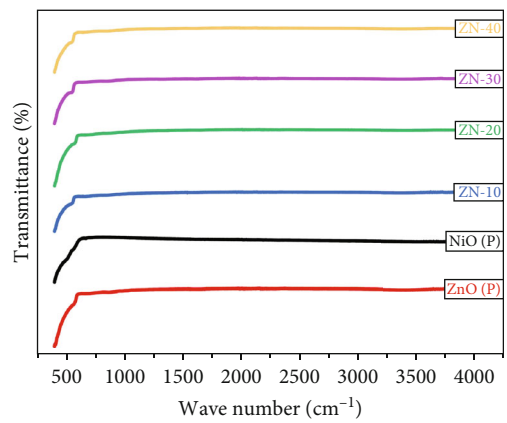

Figure 5: FTIR analysis.

ZnO and NiO are relatively small as compared to that of ZN-30. This increased absorption for ZN-30 is the confirmation point that confirms the formation of a heterojunction between ZnO and NiO. Figures 6(b)–6(d) represent the Tauc's plot that were evaluated for obtaining the band gap energy values of the samples that were observed to be 3.26 eV for ZnO, 3.8 eV for NiO, and 3.4 eV for ZN-30 heterojunction [38, 39].

3.6. Photocatalytic H_2 Production, H_2 Production Rate, and Photostability. The photocatalytic activity of the samples is shown in Figure 7(a), from which we can conclude that the photocatalytic activity of ZnO is low as compared to NiO and its heterojunctions [27], while for the heterojunctions, the photocatalytic activity is enhanced. The best performance is shown by ZN-30 heterojunction with the highest response. Here, the most efficient heterojunction is formed which results in the enhanced photocatalytic activity. The reason for this enhanced activity is the ZnO–NiO ratio. As it can be seen from Figure 7(a), when the amount of NiO is increased, the H_2 production response is increased [28]. But up to a certain point, the photocatalytic activity increases, after which it starts to decreases, which is due to the shielding effect, i.e., large content of ZnO on the surface of NiO, which almost absorbs all the light and less light is

Table 4: FTIR quantitative analysis.

Elements	Peaks	Assignments
ZnO	(a) 568 cm^{-1} (b) 1242 cm^{-1} (c) 3428 cm^{-1}	(a) Stretching vibrations (b) Bending vibrations of O-H (c) O-H stretching vibrations
NiO	(a) 575 cm^{-1} (b) 1235 cm^{-1} (c) 3497 cm^{-1}	(a) Stretching vibrations (b) Bending vibrations (c) O-H stretching vibrations on the surface
ZN-30	(a) 563 cm^{-1} (b) 570 cm^{-1}	(a) ZnO characteristics (b) NiO characteristics

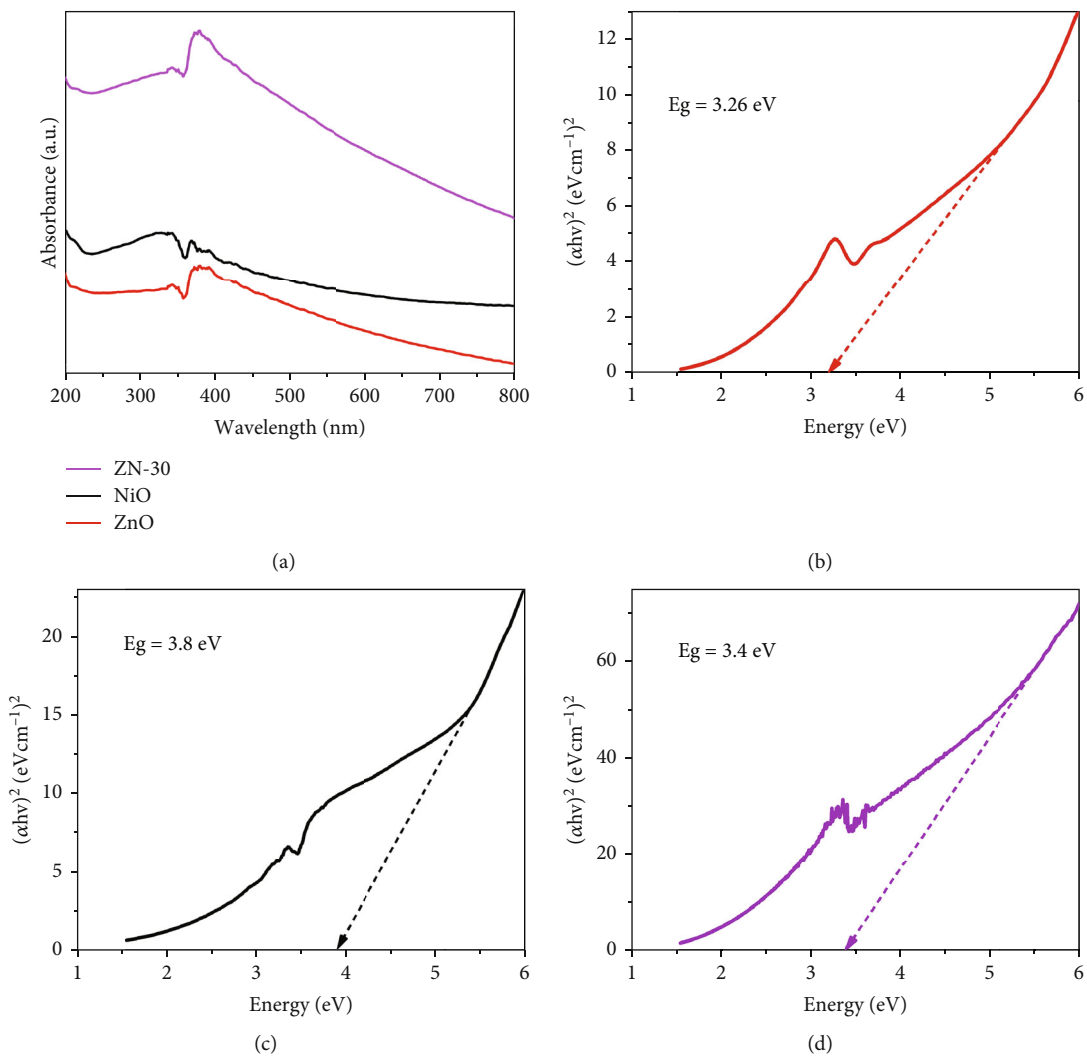

Figure 6: UV-Vis analysis. (a) Absorption spectra, (b) ZnO Tauc plot, (c) NiO Tauc plot, and (d) ZN-30 Tauc plot.

reached to NiO. H_2 production rates of the samples are illustrated in Figure 7(b), according to which ZnO exhibits good H_2 production rates (168.91 $\mu mol g^{-1} h^{-1}$) as compared to NiO (135.78 $\mu mol g^{-1} h^{-1}$). The best production rates were observed for ZN-30 (247.56 $\mu mol g^{-1} h^{-1}$) which is 1.46 times greater than ZnO and 1.82 times greater than NiO. Figure 7(c) illustrates the cyclic stability of ZN-30, according to which when the catalyst is exposed to light (xenon light) for continuous five cycles (each of five hours), the fluctuation in the H_2 production activity is of very small order and is almost negligible showing a good cyclic stability and reduced resistance corrosion.

3.7. Transient Photocurrent, EIS, and Photoluminescence Analysis. The transient photocurrent analysis of the samples was conducted in order to study the photogenerated charge

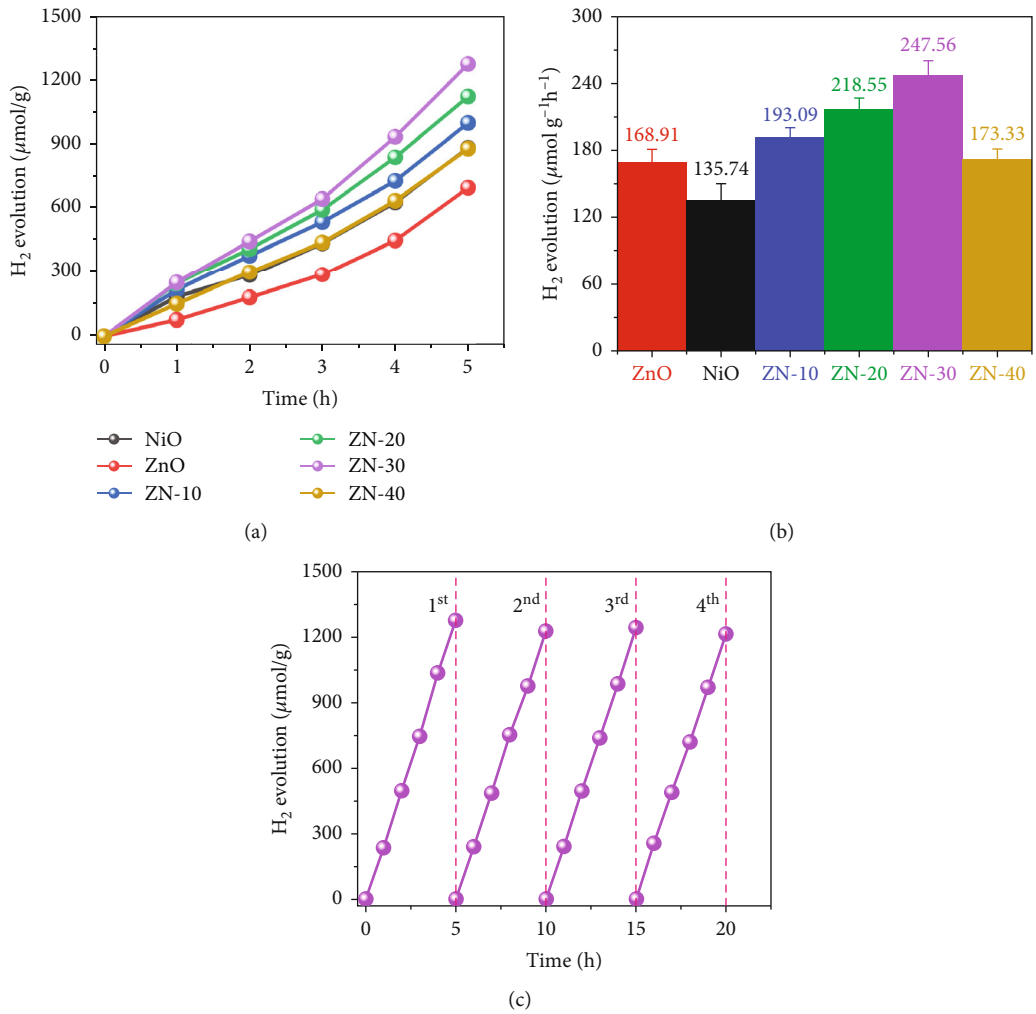

Figure 7: (a) Photocatalytic H2 production, (b) H2 production rate, and (c) photostability.

carrier intensity as shown in Figure 8(a). The transient photocurrent analysis implies that the photogenerated charge carrier's intensity in both ZnO and NiO is less, as they are in their pure form, but for ZN-30, the photogenerated charge carrier's intensity is highly increased, which is due to the formation of a heterojunction, therefore enhancing its photocatalytic activity. The electrochemical impedance spectroscopy is illustrated in Figure 8(b), which implies that NiO has a bigger circular arc's diameter, whereas ZnO has the 2nd largest circular arc's diameter, which means it has a higher charge transfer resistance as compared to ZN-30, as they are in pure form. ZN-30, being a heterojunction, has a smaller circular arc's diameter among ZnO and NiO, which implies that ZN-30 has the lowest charge transfer resistance (through the interface) which promotes fast interfacial charge transfer that is superlative to photocatalytic activity [27, 30]. The photoluminescence analysis is illustrated in Figure 8(c). In the PL spectra, the excitation wavelength of 260 nm was applied. The micrograph indicates that NiO has the highest emission intensity. The second highest emission intensity is observed for ZnO. For ZN-30, the emission intensity is the lowest, which indicated the suppression of electron-hole pair recombination. From the above results, we can state that for ZN-30, the photogenerated charge carrier's intensity is highly increased, the charge transfer resistance is low as a result promoting fast interfacial charge transfer, and the electron-hole pair recombination is successfully suppressed (for ZN-30), all of which are highly in favor of efficient photocatalysis.

3.8. Proposed Mechanism. We have presented a mechanism for the working of the photocatalyst that explains a clear-cut image of the whole process. When light is radiated on ZnO nanoparticles, the electrons (e^-) in the valance band of ZnO jump to the conduction band leaving a hole (h^+) behind [40]; due to the low charge transfer resistance in the heterojunction (through the interface), the electrons are transferred to the surface of NiO, therefore increasing the electron concentration on the surface of NiO, whereas the hole concentration is greater on the other side (ZnO); as a result, a depletion layer is formed which helps in a good electron-hole pair separation. This process occurring is called internal electric field-induced charge transfer. Similarly, at the same time, the redox reaction occurs. On the surface of NiO, reduction reaction occurs; H^+ ions receive electrons from the surface of NiO and produce H_2

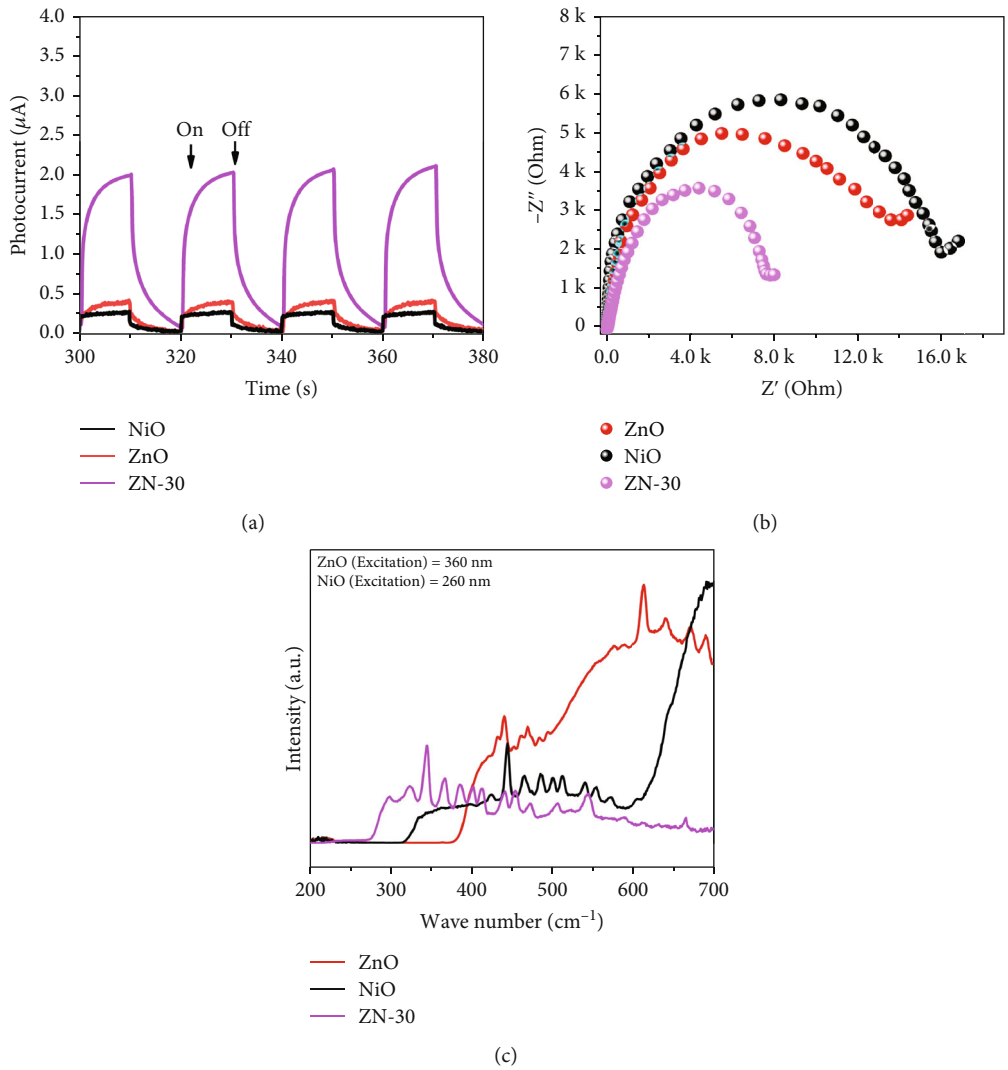

Figure 8: (a) Transient photocurrent, (b) EIS, and (c) PL analysis.

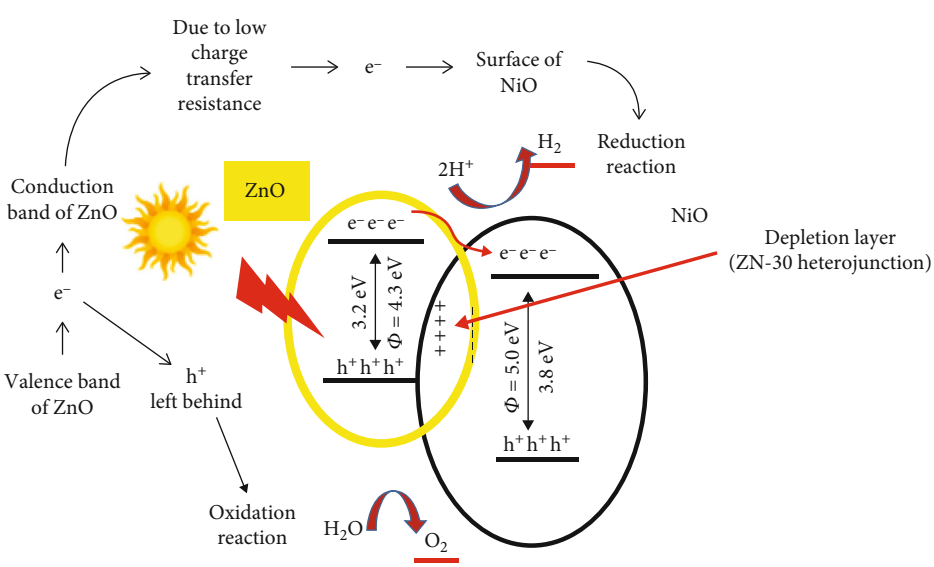

Figure 9: Proposed mechanism.

molecules. Similarly, the holes that were left behind participate in the oxidation reaction to produce oxygen molecules from O^- ions. Here, both of these reactions (reduction and oxidation) occur simultaneously and a charge balance is maintained [22]; as a result, we obtain H_2 along with O_2 as illustrated in Figure 9.

4. Conclusion

ZnO (nanoplateletes), NiO (nanospheres), and ZnO/NiO (nanoplateletes on the surface of nanospheres) heterojunctions were successfully synthesized by hydrothermal method. XRD, SEM, EDX, FTIR, and UV-visible analyses were adapted to confirm the formation of our required samples. The band gaps estimated from UV-Vis analysis for ZnO and NiO are 3.26 eV and 3.8 eV, respectively, whereas for ZN-30 heterojunction, the band gap value was 3.4 eV, which is suitable for photocatalytic hydrogen production. The electrochemical results revealed that transient photocurrent response of ZN-30 is greater than pristine ZnO, NiO, and rest of the heterojunctions, with a lower charge transfer resistance, therefore allowing for fast interfacial charge transfer, as a result enhancing the redox reactions for better photocatalysis. PL analysis indicated that the recombination of charge carrier's is highly suppressed in ZN-30 heterojunction. Based on these results, the photocatalytic H_2 production of all the heterojunctions is increased. The utmost H_2 production is achieved by ZN-30 with H_2 production rates of 247.56 $\mu mol g^{-1} h^{-1}$ which is 1.46 times greater than ZnO and 1.82 times greater than NiO. Therefore, the photocatalytic H_2 production response is enhanced.

Data Availability

Data are available from the authors and will be provided if needed.

Conflicts of Interest

The authors declare no conflicts of interests.

Acknowledgments

We have carried out this research self-funded.

References

[1] B. Ekwurzel, J. Boneham, M. W. Dalton et al., "The rise in global atmospheric CO_2, surface temperature, and sea level from emissions traced to major carbon producers," *Climatic Change*, vol. 144, no. 4, pp. 579–590, 2017.

[2] F. Dawood, G. Shafiullah, and M. Anda, "A hover view over Australia's hydrogen industry in recent history: the necessity for a hydrogen industry knowledge-sharing platform," *International Journal of Hydrogen Energy*, vol. 45, no. 58, pp. 32916–32939, 2020.

[3] L. J. J. E. Nunes, "The rising threat of atmospheric CO_2: a review on the causes, impacts, and mitigation strategies," *Environments*, vol. 10, no. 4, p. 66, 2023.

[4] H. Nazir, N. Muthuswamy, C. Louis et al., "Is the H_2 economy realizable in the foreseeable future? Part III: H_2 usage technologies, applications, and challenges and opportunities," *International Journal of Hydrogen Energy*, vol. 45, no. 53, pp. 28217–28239, 2020.

[5] Z. Y. Yu, Y. Duan, X. Y. Feng, X. Yu, M. R. Gao, and S. H. Yu, "Clean and affordable hydrogen fuel from alkaline water splitting: past, recent progress, and future prospects," *Advanced Materials*, vol. 33, no. 31, article 2007100, 2021.

[6] D. V. César, R. F. Robertson, and N. S. Resende, "Characterization of ZnO and TiO_2 catalysts to hydrogen production using thermoprogrammed desorption of methanol," *Catalysis Today*, vol. 133, pp. 136–141, 2008.

[7] W.-C. Lin, W. D. Yang, I. L. Huang, T. S. Wu, and Z. J. Chung, "Hydrogen Production from Methanol/Water Photocatalytic Decomposition Using Pt/TiO2−xNxCatalyst," *Energy & Fuels*, vol. 23, no. 4, pp. 2192–2196, 2009.

[8] A. Pérez-Larios, R. Lopez, A. Hernández-Gordillo, F. Tzompantzi, R. Gómez, and L. M. Torres-Guerra, "Improved hydrogen production from water splitting using TiO_2-ZnO mixed oxides photocatalysts," *Fuel*, vol. 100, pp. 139–143, 2012.

[9] S. T. Kochuveedu, Y. H. Jang, and D. H. Kim, "A study on the mechanism for the interaction of light with noble metal-metal oxide semiconductor nanostructures for various photophysical applications," *Chemical Society Reviews*, vol. 42, no. 21, pp. 8467–8493, 2013.

[10] A. Fujishima, X. Zhang, and D. A. Tryk, "TiO_2 photocatalysis and related surface phenomena," *Surface Science Reports*, vol. 63, no. 12, pp. 515–582, 2008.

[11] G. Tian, Y. Chen, W. Zhou et al., "3D hierarchical flower-like TiO 2 nanostructure: morphology control and its photocatalytic property," *CrystEngComm*, vol. 13, no. 8, pp. 2994–3000, 2011.

[12] T. Zhu, J. Li, and Q. Wu, "Construction of TiO2Hierarchical nanostructures from nanocrystals and their photocatalytic properties," *ACS Applied Materials & Interfaces*, vol. 3, no. 9, pp. 3448–3453, 2011.

[13] C. Chen, J. Liu, P. Liu, and Y. Benhai, "Investigation of photocatalytic degradation of methyl orange by using nano-sized ZnO catalysts," *Advances in Chemical Engineering and Science*, vol. 1, no. 1, pp. 9–14, 2011.

[14] F. Lu, W. Cai, and Y. Zhang, "ZnO hierarchical micro/nanoarchitectures: solvothermal synthesis and structurally enhanced photocatalytic performance," *Advanced Functional Materials*, vol. 18, no. 7, pp. 1047–1056, 2008.

[15] A. Mclaren, T. Valdes-Solis, G. Li, and S. C. Tsang, "Shape and size effects of ZnO nanocrystals on photocatalytic activity," *Journal of the American Chemical Society*, vol. 131, no. 35, pp. 12540-12541, 2009.

[16] L. Xu, H. Yan-Ling, C. Pelligra et al., "ZnO with different morphologies synthesized by solvothermal methods for enhanced photocatalytic activity," *Chemistry of Materials*, vol. 21, no. 13, pp. 2875–2885, 2009.

[17] M. Irfan, S. Afzal, M. Hussain et al., "Testing of Sr-Doped ZnO/CNT Photocatalysts for Hydrogen Evolution from Water Splitting under Atmospheric Dielectric Barrier Plasma Exposure," *ACS Omega*, vol. 8, no. 21, pp. 18891–18900, 2023.

[18] M. Ahmad, S. Yingying, A. Nisar et al., "Synthesis of hierarchical flower-like ZnO nanostructures and their functionalization by Au nanoparticles for improved photocatalytic and high

performance Li-ion battery anodes," *Journal of Materials Chemistry*, vol. 21, no. 21, pp. 7723–7729, 2011.

[19] C. C. Hsu and N. L. Wu, "Synthesis and photocatalytic activity of ZnO/ZnO2 composite," *Journal of Photochemistry and Photobiology A: Chemistry*, vol. 172, no. 3, pp. 269–274, 2005.

[20] D. L. Liao, C. A. Badour, and B. Q. Liao, "Preparation of nanosized TiO2/ZnO composite catalyst and its photocatalytic activity for degradation of methyl orange," *Journal of Photochemistry and Photobiology A: Chemistry*, vol. 194, no. 1, pp. 11–19, 2008.

[21] R. Liu, Y. Huang, A. Xiao, and H. Liu, "Preparation and photocatalytic property of mesoporous ZnO/SnO2 composite nanofibers," *Journal of Alloys and Compounds*, vol. 503, no. 1, pp. 103–110, 2010.

[22] F. Tian and Y. Liu, "Synthesis of p-type NiO/n-type ZnO heterostructure and its enhanced photocatalytic activity," *Scripta Materialia*, vol. 69, no. 5, pp. 417–419, 2013.

[23] G. S. Sree, S. M. Botsa, B. J. M. Reddy, and K. V. B. Ranjitha, "Enhanced UV–Visible triggered photocatalytic degradation of Brilliant green by reduced graphene oxide based NiO and CuO ternary nanocomposite and their antimicrobial activity," *Arabian Journal of Chemistry*, vol. 13, no. 4, pp. 5137–5150, 2020.

[24] X. Wang, J. Song, L. Gao, J. Jin, H. Zheng, and Z. Zhang, "Optical and electrochemical properties of nanosized NiO via thermal decomposition of nickel oxalate nanofibres," *Nanotechnology*, vol. 16, no. 1, p. 37, 2004.

[25] A. Hameed, T. Montini, V. Gombac, and P. Fornasiero, "Photocatalytic decolourization of dyes on NiO–ZnO nanocomposites," *Photochemical & Photobiological Sciences*, vol. 8, pp. 677–682, 2009.

[26] J. M. Nel, F. D. Auret, L. Wu, M. J. Legodi, W. E. Meyer, and M. Hayes, "Fabrication and characterisation of NiO/ZnO structures," *Sensors and Actuators B: Chemical*, vol. 100, no. 1-2, pp. 270–276, 2004.

[27] S. Yousaf, S. Zulfiqar, M. I. Din et al., "Solar light irradiated photocatalytic activity of ZnO–NiO/rGO nanocatalyst," *Journal of Materials Research and Technology*, vol. 12, pp. 999–1009, 2021.

[28] U. S. Udayachandran Thampy, A. Mahesh, K. S. Sibi, I. N. Jawahar, and V. Biju, "Enhanced photocatalytic activity of ZnO–NiO nanocomposites synthesized through a facile sonochemical route," *SN Applied Sciences*, vol. 1, pp. 1–15, 2019.

[29] R. K. Sharma, D. Kumar, and R. Ghose, "Synthesis of nanocrystalline ZnO–NiO mixed metal oxide powder by homogeneous precipitation method," *Ceramics International*, vol. 42, no. 3, pp. 4090–4098, 2016.

[30] L. Ma, X. Ai, Y. Chen et al., "Improved photocatalytic activity via N-type ZnO/p-type NiO heterojunctions," *Nanomaterials*, vol. 12, no. 20, p. 3665, 2022.

[31] N. Jayababu, M. Poloju, J. Shruthi, and M. R. Reddy, "Synthesis of ZnO/NiO nanocomposites for the rapid detection of ammonia at room temperature," *Materials Science in Semiconductor Processing*, vol. 102, article 104591, 2019.

[32] M. Xiao, Y. Lu, Y. Li, H. Song, L. Zhu, and Z. Ye, "A new type of p-type NiO/n-type ZnO nano-heterojunctions with enhanced photocatalytic activity," *RSC Advances*, vol. 4, no. 65, pp. 34649–34653, 2014.

[33] N. R. Reddy, P. M. Reddy, J. H. Jung, and S. W. Joo, "Construction of various morphological ZnO-NiO S-scheme nanocomposites for photocatalytic dye degradation," *Inorganic Chemistry Communications*, vol. 146, article 110107, 2022.

[34] N. D. J. A. M. S. Dien, "Preparation of various morphologies of ZnO nanostructure through wet chemical methods," *Advances in Materials Science*, vol. 4, pp. 1–5, 2019.

[35] H. D. Weldekirstos, B. Habtewold, and D. M. Kabtamu, "Surfactant-assisted synthesis of NiO-ZnO and NiO-CuO nanocomposites for enhanced photocatalytic degradation of methylene blue under UV light irradiation," *Frontiers in Materials*, vol. 9, article 832439, 2022.

[36] A. Moulahi, F. Sediri, and N. Gharbi, "Hydrothermal synthesis of nanostructured zinc oxide and study of their optical properties," *Materials Research Bulletin*, vol. 47, no. 3, pp. 667–671, 2012.

[37] G. Anandha Babu, "An investigation of flower shaped NiO nanostructures by microwave and hydrothermal route," *Journal of Materials Science: Materials in Electronics*, vol. 25, pp. 5231–5240, 2014.

[38] N. R. Yogamalar and A. Chandra Bose, "Absorption-emission study of hydrothermally grown Al:ZnO nanostructures," *Journal of Alloys and Compounds*, vol. 509, no. 34, pp. 8493–8500, 2011.

[39] N. K. Yetim, N. Aslan, A. Sarıoğlu, N. Sarı, and M. M. Koç, "Structural, electrochemical and optical properties of hydrothermally synthesized transition metal oxide (Co_3O_4, NiO, CuO) nanoflowers," *Journal of Materials Science: Materials in Electronics*, vol. 31, no. 15, pp. 12238–12248, 2020.

[40] G. S. Sree, B. S. Mohan, B. J. Reddy, and K. V. Ranjitha, "Deterioration of Cadmium and pathogens from contaminated water using hydrothermally prepared NiO-ZnO-RGO composite," *Journal of Materials Research and Technology*, vol. 18, no. 10, pp. 976–987, 2021.